ADVANCED MATERIALS
www.advmat.de

Construction of MnO_2 Artificial Leaf with Atomic Thickness as Highly Stable Battery Anodes

Binbin Jia, Wenxing Chen, Jun Luo, Zhao Yang, Lidong Li, and Lin Guo**

The leaf-like structure is a classic and robust structure and its unique vein support can reduce structural instability. However, biomimetic leaf structures on the atomic scale are rarely reported due to the difficulty in achieving a stable vein-like support in a mesophyll-like substrate. A breathable 2D MnO_2 artificial leaf is first reported with atomic thickness by using a simple and mild one-step wet chemical method. This homogeneous ultrathin leaf-like structure comprises of vein-like crystalline skeleton as support and amorphous microporous mesophyll-like nanosheet as substrate. When used as an anode material for lithium ion batteries, it first solves the irreversible capacity loss and poor cycling issue of pure MnO_2, which delivers high capacity of 1210 mAh g^{-1} at 0.1 A g^{-1} and extremely stable cycle life over 2500 cycles at 1.0 A g^{-1}. It exhibits the most outstanding cycle life of pure MnO_2 and even comparable to the most MnO_2-based composite electrode materials. This biomimetic design provides important guidelines for precise control of 2D artificial systems and gives a new idea for solving poor electrochemical stability of pure metal oxide electrode materials.

2D materials have achieved significant advantages in some applications, due to their unique structural characteristics and relevant physicochemical properties.[1–7] In fact, 2D nanostructures also widely exist in biological materials and generate some amazing functionalities, which offers us great opportunities to further expand the species and applications of 2D biomimetic nanomaterials.[8–13] Leaf-like structure is a classic and robust 2D structure and the cross-linked vein support can effectively enhance the structural stability. To date, some research efforts have been carried out to simulate artificial leaf systems in functionalities.[14,15] For example, Yang and co-workers functionally imitated photosynthesis and induced the self-photosensitization of a nonphotosynthetic bacterium with cadmium sulfide nanoparticles, enabling the photosynthesis of acetic acid from carbon dioxide.[16] However, morphology and structure bionics process on atomic scale are rarely reported, because it is difficult to achieve a stable vein-like support in the ultrathin mesophyll-like substrate. For inorganic materials, the introduction of nonflexible crystalline support into amorphous atomic thick sheet might be a possible solution to construct this leaf-like nanostructure. Based on layer growth theory,[17] if the structure of a regular ultrathin nanosheet is amorphous, it would also have a certain roughness produced by fluctuation. In the wrinkled area, many monomolecular steps are presented. This stepped structure contains a high concentration of kinks, which become the most favorable growth position to be filled up by the next coming molecules. Subsequently, those kinks serve as crystal seeds to further grow along the steps layer by layer, and finally grow into a crystal skeleton structure along those wrinkled steps (**Figure 1**a). The final product is a leaf-like porous amorphous/crystalline 2D homogeneous structure. It comprises of ultrathin flexible amorphous sheet as mesophyll, nonflexible crystal skeleton as a vein, and porous structure as a breathable stoma (Figure 1b).

It is well known that pure metal oxides have been synthesized and applied to improve performance of batteries, because they can in principle deliver high capacity compared to currently used graphite materials.[18–25] Among these metal oxides, MnO_2, as an environmentally friendly material, is abundant in the Earth's crust and possesses a high theoretical capacity (about 1232 mAh g^{-1}) as an anode material for lithium ion batteries (LIBs). The synthesis of MnO_2-based composite materials have already scored great success for energy storage applications.[26,27] However, the practical applications of pure MnO_2 anode materials are usually limited by the low reversible capacity, poor cycling performance, because they usually suffer from large volume changes during repeated lithium uptake and removal reactions, which cause local stress and eventually lead to electrode failure.[28] The leaf-like structure design with natural vein-like mechanic support

Dr. B. Jia, Dr. Z. Yang, Prof. L. Li, Prof. L. Guo
School of Chemistry
Beijing Advanced Innovation Center for Biomedical Engineering
Beihang University
Beijing 100191, China
E-mail: lilidong@buaa.edu.cn; guolin@buaa.edu.cn
Prof. W. Chen
Beijing Key Laboratory of Construction Tailorable Advanced Functional Materials and Green Applications
School of Materials Science and Engineering
Beijing Institute of Technology
Beijing 100081, China
Prof. J. Luo
Center for Electron Microscopy
Institute for New Energy Materials
Tianjin University of Technology
Tianjin 300384, China
The ORCID identification number(s) for the author(s) of this article can be found under https://doi.org/10.1002/adma.201906582.

DOI: 10.1002/adma.201906582

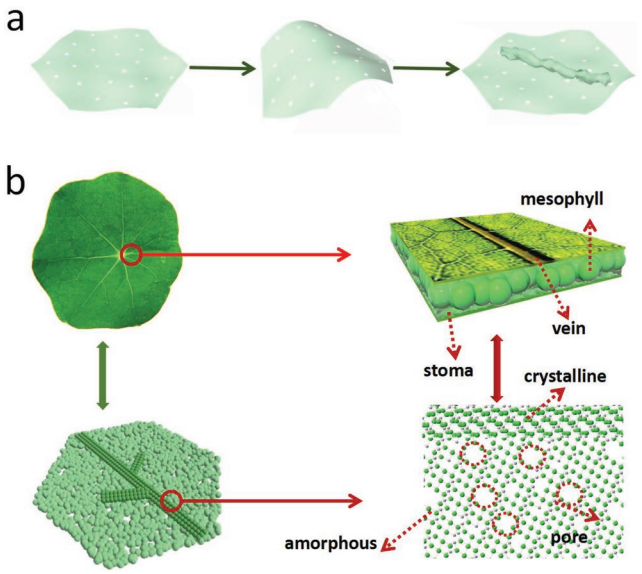

Figure 1. a) Construction of crystal skeleton on amorphous nanosheets. b) Illustration of the breathable artificial leaves structure.

would be an effective strategy to solve this instablility problem of MnO_2 anode materials.

In this work, we first develop a simple and rapid synthetic route to construct a breathable 2D MnO_2 artificial leaf with atomic thickness (b-MnO_2 ALAT). The 2D homogeneous structure comprises of flexible ultrathin amorphous sheet as mesophyll to promote ion transport, nonflexible crystal skeleton as a vein to provide a stable mechanical support, and porous structure as a breathable stoma to accelerate ion transport rate. This unique amorphous/crystalline leaf-like design leads to significant improvement on capacity and cycling life of LIBs. It delivers extremely high reversible capacities of 1210 mAh g^{-1} at 0.1 A g^{-1} as a pure MnO_2 material, presents excellent rate capability, and especially, exhibits ultralong cycling stability, which shows almost no capacity fading after 2500 cycles. This electrochemical stability largely outperforms previously reported pure MnO_2 anode materials, and even comparable to those MnO_2-based composite materials.

The detailed structure of b-MnO_2 ALAT is displayed in **Figure 2**. Transmission electron microscopy (TEM) images (Figure 2a,b) reveal a regular hexagonal nanosheet with a diameter of ≈320 nm and vein-like skeleton structure embedded at the center. High-resolution TEM (HRTEM) results (Figure 2c) indicate that the vein-like skeleton structure is crystalline, where the identified lattice spacing of 0.24 nm can be assigned to the (-111) facets of MnO_2, which is in agreement with the X-ray diffraction (XRD) results (Figure S1, Supporting Information). Interestingly, no fringe lattices can be observed for the rest part of nanosheet, indicating its amorphous nature. To further prove our suggestion, detailed structural features are characterized by employing high-angle annular dark-field scanning transmission electron microscopy (HAADF-STEM) (Figure 2d–f).

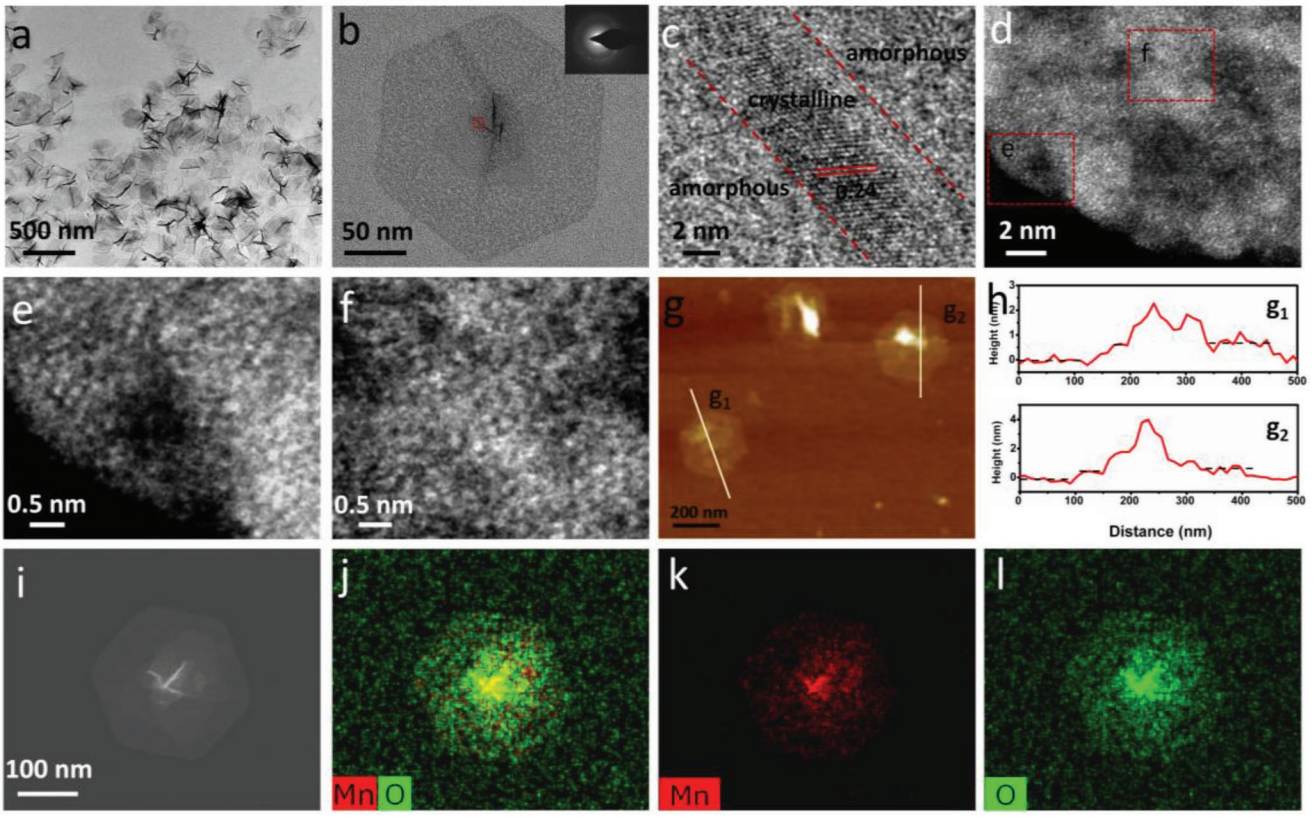

Figure 2. a,b) TEM images of b-MnO_2 ALAT (the inset of (b) shows the corresponding selected-area electron-diffraction pattern). c) HRTEM image of b-MnO_2 ALAT. d) HAADF-STEM images of b-MnO_2 ALAT. e,f) HAADF-STEM images of b-MnO_2 ALAT corresponding to different framed regions çnolayer in (d). g) AFM image of b-MnO_2 ALAT. h) Height images of b-MnO_2 ALAT. i–l) Corresponding elemental mapping analyses of b-MnO_2 ALAT.

The STEM measurements also reveal that the atoms of surrounding nanosheet are disordered. Of note, 1–2 nm dense micropores are also detected on individual MnO_2 nanosheet (Figure S2, Supporting Information). Measured by atomic force microscopy (AFM) (Figure 2g,h), the thicknesses of skeleton-like support and surrounding amorphous monolayer are ≈2–4 and 0.6 nm, respectively. The corresponding elemental mapping analyses (Figure 2i–l) reveal that Mn and O are homogeneously distributed across the whole nanosheet.

In order to investigate growth mechanism of MnO_2-sample, a time resolved ex situ TEM investigation was performed. The growth mechanism includes following three steps. First, dissociative amorphous nanoclusters (Figure S3, Supporting Information) start to assemble and tend to form small nanoplates with porous structure (**Figure 3**a). Due to the random aggregation of nanoparticles, the nanoplates possess amorphous structure with an pore size about 5 nm (Figure 3a$_1$). At this stage, the zeta potentials (Figure S4, Supporting Information) are measured to be −14 mV, suggesting the fragile and unstable feature of primary porous nanosheets.[29] Therefore, it has a tendency to detach from the primary matrix for lowering their overall energy. Besides, the shape of the primary pores is relatively irregular, which is considered to be unstable, according to the Kelvin equation.[30] Second, at the most favorable growth positions, those ultrathin amorphous nanoplates tend to crystallize. In details, when the proceeding reaction continued, epitaxial layers form within picoseconds along with a rapid alignment arising from mechanical relaxation of the highly stressed interface. These interfaces are formed upon initial contact between amorphous nanoparticles, which are orderly distributed on the edge of nanoplates (Figure 3b). Meanwhile, the reconstruction process causes to shrinkage of large pores (Figure 3b$_1$), further producing ultrathin nanosheets with evenly distributed nanopores. According to the layer growth theory, nanosheets are easy to bend in the stirred solution. Those wrinkled lines are composed of high concentration of kinks, which serve as the most favorable growth positions.[17] Due to principle of minimum energy, the next coming MnO_2 molecules tend to line up along those wrinkled steps and form vein-like crystalline skeleton during the reconstruction process. To prove our assumptions, we carried out a series of control experiments by increasing the mass of $KMnO_4$. When the mass of $KMnO_4$ increased to 60 mg, a nanoflower-like hierarchical structure was obtained (Figure S5, Supporting Information). Third, nanosheet keeps growing until they are large enough to reach a certain boundary. At this time, nanosheets with small and well-distributed micropores (Figure 3c,c$_1$) become very stable with the lowest zeta potential of −40 mV (Figure S4, Supporting Information), suggesting successful synthesis of b-MnO_2 ALAT.

The chemical state and local atomic structure of our sample are studied by X-ray photoelectron spectroscopy (XPS) and X-ray absorption near-edge spectroscopy (XANES). As shown in Figure S6a in the Supporting Information, Mn $2p_{3/2}$ and Mn $2p_{1/2}$ peaks are located at 642.2 and 654.1 eV respectively, which can be ascribed to a large number of Mn^{4+} ions presented in the sample. The general Mn oxidation state can be further confirmed by the binding energy width (ΔE) between the separated Mn 3s peaks (Figure S6b, Supporting Information). By reference to the ΔE values of 5.79, 5.50, 5.41, and 4.78 eV acquired from standard samples of MnO, Mn_3O_4, Mn_2O_3, and MnO_2, respectively, the binding energy (ΔE = 4.95 eV) of our sample suggests that the valence of Mn element is between +3 and +4.[31] Figure 3d shows K-edge XANES spectra and some standard materials including MnO, Mn_3O_4, Mn_2O_3, bulk-MnO_2, and $KMnO_4$ for reference. The average oxidation state of Mn can be described by establishing a linear relationship between K-edge energy and Mn oxidation state (Figure 3e). The results show that the average oxidation state of Mn is 3.82. The absorption edge of sample is shifted to lower energy about 1 eV, which suggests the existence of mixed oxidation states of Mn^{3+}/Mn^{4+} compared to bulk-MnO_2.[32] R-space spectra is also measured to investigate the local atomic arrangements around Mn atoms (Figure 3f; Table S1, Supporting Information). Compared to the peaks for bulk-MnO_2, the significant decrease of Mn–O and slight increase of Mn–Mn indicate less Mn–O coordination and more Mn–Mn coordination presented in our sample, respectively. As a result, a certain degree of metallicity happened in our sample, leading to enhanced electrical conductance. Meanwhile, k-space spectra of MnO_2-sample and bulk MnO_2 were also conducted to study the structural details (Figure 3g). The results suggest that our sample exists a certain degree of amorphization and a lower average Mn oxidation state. Based on the previous report, the existence of Mn^{3+} ions may increase charge storage capacitance of MnO_2.[33] Thus, 2D amorphous/crystalline structure and a certain amount of Mn^{3+} sites are expected to dramatically alter its electronic structure and increase electron transfer efficiency, which would provide great performance as an electrode material.

The electrochemical performance of b-MnO_2 ALAT as an anode material for LIBs is thoroughly evaluated, as well as amorphous MnO_2 nanosheets (a-MnO_2) and crystalline MnO_2 nanosheets (c-MnO_2) for comparison (Figures S7–S11, Supporting Information). Figure S12 in the Supporting Information shows the cyclic voltammetry (CV) curves of b-MnO_2 ALAT during initial three cycles recorded at a scan rate of 0.1 mV s^{-1}. It can be seen that upon the first scan, three cathodic peaks appear at 1.5, 0.9, and 0.2 V, corresponding to the a two-step possible reduction process $Mn^{3+/4+}$ to Mn^{2+}, Mn^{2+} to Mn, and the formation of a solid electrolyte interphase (SEI) layer, respectively. Two anodic peaks located at 1.1 and 1.9 V are observed, which indicates that the reoxidation of manganese may need two steps. During the second cycle, the cathodic peaks at 1.5 and 0.9 V disappear and the peak in the low potential region shifts from 0.2 to 0.3 V, suggesting an irreversible structural or textural change in the electrode materials. The CV curve of the third scan closely resembles that of the second scan, which manifests that the lithiation and delithiation processes are highly reversible from the second cycle onwards.[34] Figure S13 in the Supporting Information shows the cycling performance at a current density of 0.1 A g^{-1}. It is found that the specific capacity undergoes an obvious drop from 1st to 80th cycle. And then the capacity is reactivated to 1210 mAhg^{-1} at the 450th cycle, more than 310% capacity recovery from the lowest value at the same rate. This similar phenomenon of rising has been also reported previously on metal oxide electrodes (amorphous Fe_2O_3,[35] amorphous Cr_2O_3,[36] crystalline Fe_3O_4,[37] crystalline Co_3O_4[38]), but the magnitude and scale of the capacity rise in our work is extraordinarily large. In order to elucidate

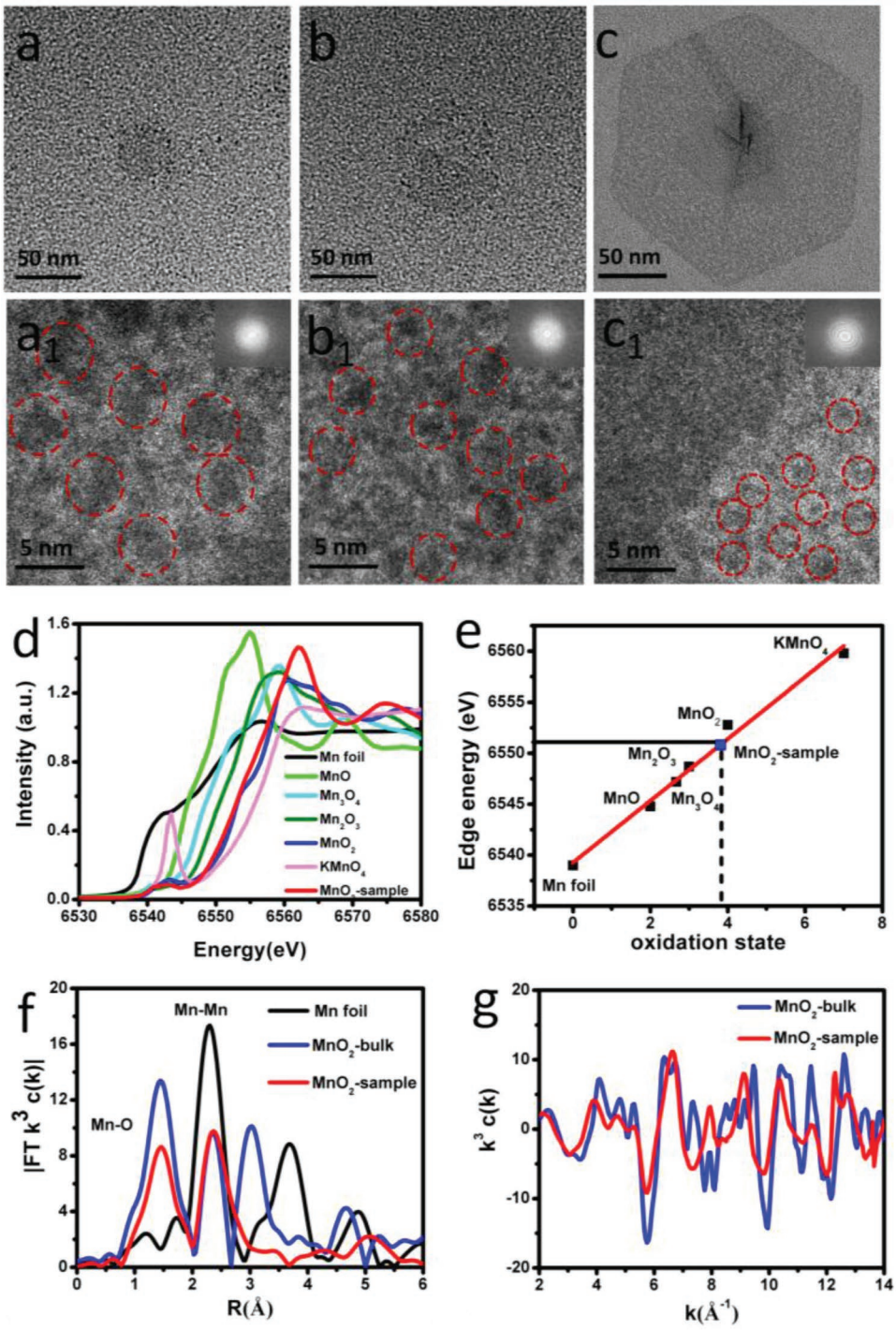

Figure 3. a–c) TEM images of the intermediate product at different reaction times. a) 5 s, b) 10 s, c) 5 min. (a_1–c_1) Corresponding HAADF-STEM images of the intermediate products at different reaction times: (a_1) 5 s, (b_1) 10 s, (c_1) 5 min. d) XANES spectra of our sample and some standard materials including MnO, Mn_3O_4, Mn_2O_3, MnO_2, and $KMnO_4$. e) Average oxidation state of Mn for samples and standards derived from K-edge energy. f) Mn K-edge EXAFS oscillation function $k^2\chi(k)$. g) Magnitude of k^2-weighted Fourier transforms of Mn edge EXAFS spectra.

capacity rise, charge–discharge profiles with different cycles are shown in Figure S14 in the Supporting Information. The discharge platforms at 0.3 and 1.1 V become inconspicuous in the process of capacity faded. On the contrary, discharge platforms become obvious during subsequent capacity rising process due to the activation of internal materials. In order to verify above results, CV curves after 5 and 500 cycles at a scan rate of 0.1 mV s^{-1} are shown in Figure S15 in the Supporting Information. The current intensities of the cathodic and anodic peaks increase significantly, which are in good agreement with

the charge–discharge curves. Interestingly, the reaction corresponding to the upturn at ≈2.8–3.0 V observed in the CVs also contributes to the capacity increase after 500 cycles. This voltage range coincides with the oxidation potential of lithium oxide decomposition ($2Li_2O \rightarrow Li_2O_2 + 2Li^+ + 2e^-$, $E = 2.87$ V).[37,39] In order to test the composition change of the sample after cycling process, the XPS measurement was performed after 500 cycles as shown in Figure S16 in the Supporting Information. The position and line shape (sharp Mn $2p_{3/2}$ peak at 642.3 eV and Mn $2p_{1/2}$ peak at 654.0 eV) of the Mn 2p doublet indicate majority MnO_2 component. The results confirm that the composition of b-MnO_2 ALAT remains during cycling. In addition, the XRD patterns of the sample before and after 500 cycles are shown in Figure S17 in the Supporting Information. The absence of (001) and (002) diffraction peaks after being charged after 500 cycles is due to activation of the internal materials after deep charge/discharge cycles. The (-111) peak shifts to the lower angles. The calculated *d*-spacing of the (-111) plane increases from 2.4 to 2.67 Å after the fully charging and discharging process, indicating that Li-ion insertion/extraction increases the distance of (111) plane. Thus, the gradual increase in the capacity is attributed to the electrochemical reversibility of lithium oxide formation/decomposition and activation of the internal materials after deep charge/discharge cycles. The cycling performance of b-MnO_2 ALAT, a-MnO_2 nanosheets, and c-MnO_2 nanosheets at a higher current density of 1 A g^{-1} are also investigated (**Figure 4**a). It is found that the reversible capacity of c-MnO_2 directly decreased to 116 mA h g^{-1} at 1 Ag^{-1} after 200 cycles. Whereas, for a-MnO_2 sample, the same reactivation process also appeared during the first 60 cycles, which can be attributed to the flexible amorphous porous structure buffered volume change during lithium uptake and removal process, thus the capacity maintains in the first 490 cycles. However, after that, the electrode suffers a dramatic degradation with the reversible capacity remaining at only 160.6 mAh g^{-1} after 600 cycles. In comparison with a-MnO_2 nanosheets, b-MnO_2 ALAT greatly improves the structural stability, leading to remarkable enhancement of the reversible capacity. The capacity remains 520 mAh g^{-1} after 2500 cycles and degrades only 1%, showing excellent cycling performance. Correspondingly, the serious structure degradation and aggregation of c-MnO_2 after 200 cycles (Figure S18, Supporting Information) and a-MnO_2 after 600 cycles can also be observed from Figure 4b, while nanosheet structure of b-MnO_2 ALAT maintains perfectly (Figure 4c). However, the stacking form of b-MnO_2 ALAT has changed, from the initial thin layer or the less layers structure to the multilayer structure (Figure 4c; Figure S19, Supporting Information). To the best of our knowledge, it exhibits the most outstanding cycle life of pure MnO_2 and even compared with most MnO_2-based composite electrode materials ever reported (Figure 4d).[40–48] Finally, rate capacity of b-MnO_2 ALAT after 500 cycles was studied as shown in Figure 4e. When the current densities are 0.1, 0.2, 0.5, 1, and 2 A g^{-1}, the reversible capacities can be stabilized at 1210, 1030, 810, 530, and 380 mAh g^{-1}, respectively. Moreover, a high capacity of 1170 mAh g^{-1} can be recovered rapidly when the current rate is reduced again from 2 to 0.1 A g^{-1}. This complete recovery at aggressive currents implies that the electrode is not damaged and integrity of electrode maintains during cycling.

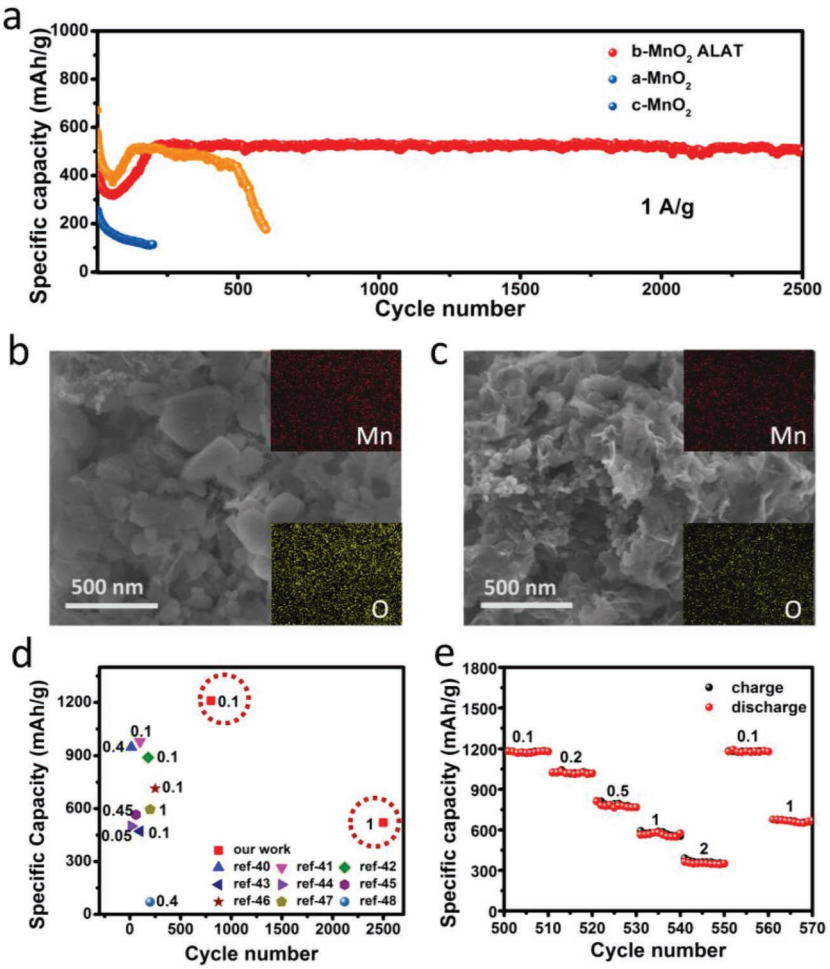

Figure 4. a) Cycling performance of b-MnO_2 ALAT at 1A g^{-1}. b) SEM image of a-MnO_2 anode after 600 cycles (the inset of (b) shows the corresponding elemental mapping analyses). c) SEM image of b-MnO_2 ALAT anode after 600 cycles (the inset of (c) shows the corresponding elemental mapping analyses). d) Comparisons of specific capacity and cycling performance between sample and previously reported MnO_2 and MnO_2-based composite electrodes. e) Rate capability of b-MnO_2 ALAT.

To illuminate electrochemical kinetics of b-MnO_2 ALAT, the CV tests at various scan rates after 500 cycles from 0.1 to 5 mV s^{-1} are carried out as shown in **Figure 5**a. Two broad peaks can be observed in both cathodic and anodic processes. It is interesting to note that the small peak separations are nearly the same when the scan rate increases from 0.1 to 2 mV s^{-1},

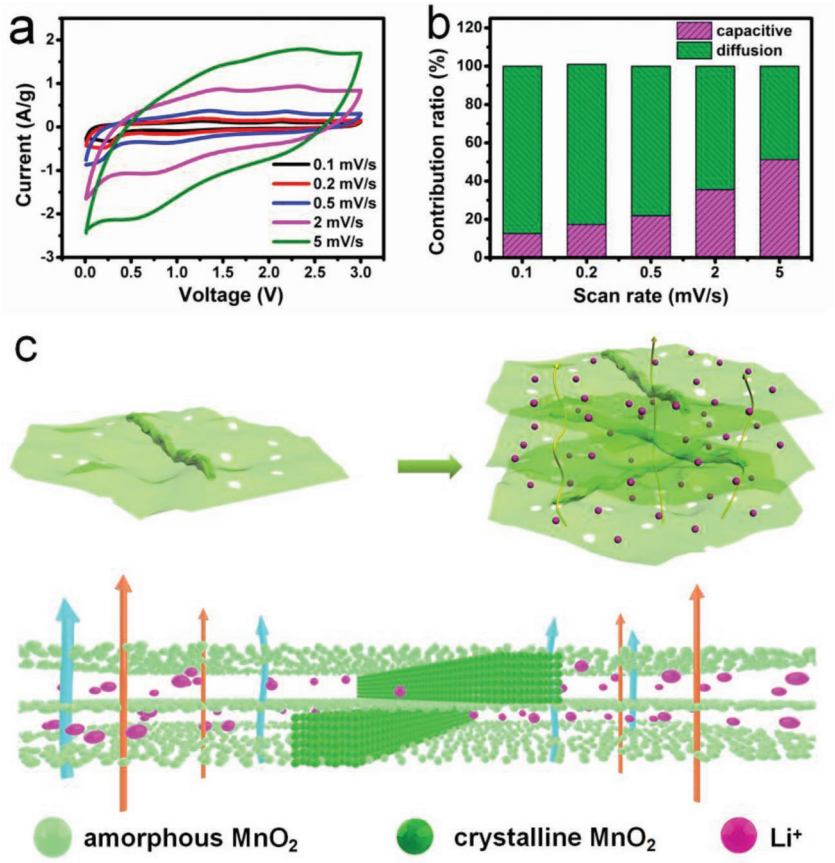

Figure 5. a) CV curves at various scan rates, from 0.1 to 2 mV s^{-1}. b) Separation of contributions from capacitive and diffusion-controlled capacities at different sweep rates. c) Schematic illustration of advantageous features of b-MnO_2 ALAT for energy storage.

implying the minimal polarization at high rates. To further analyze the intrinsic electrochemical behavior, log(*i*) change as a function of log(*v*) is plotted. The *b* values of different sweep range from 0.55 to 0.79 during the Li ions insertion process (Figure S20, Supporting Information). Meanwhile, as presented in Figure S21 in the Supporting Information, the calculated *b* values are 0.74 and 0.79 for cathodic and anodic peaks under 2 V, respectively, indicating that reaction current is derived from both diffusion-controlled process and pseudocapacitance. Based on the calculated k_1 and k_2, the capacitive (k_1v) and diffusion limited ($k_2v^{1/2}$) contributions at the fixed potentials can be analyzed in Figure 5b. As sweeping rates increase from 0.1 to 5 mV s^{-1}, the proportion of surface capacitance controlled capacity increases from 12.58% to 51.22%, while the contribution of diffusion decreases from 87.42% to 48.78%, indicating diffusion and capacitive both play a key role during the whole electrochemical process, which can be attributed to this unique porous and loosely-packing structure. Besides, the contribution of capacitive charge storage may be attributed to the large specific surface area, which provided sufficient active sites for electrochemical Li ion intercalation and deintercalation, as well as cluster gaps or interstitial sites for lithium storage.

Above all, we propose the following three points to explain the excellent cycling performance and high capacity (Figure 5c). First, 2D nanostructures with large surface area helps to accommodate the volume changes associated with electrochemical reactions. Second, porous amorphous structures ensure the effective wetting and penetration of electrolyte to the electrode surface, offer continuous charge transport pathway, shorten ion diffusion distance, and buffer volume changes, thus suppress the powdering and peeling problems suffered from the structure degradation. Third, this unique 2D interconnected structure with thickened vein-like crystalline support greatly improves the stability, and perfectly solves the closely stacking problem of 2D ultrathin nanosheets. It will leave a small inter space between overlapped nanosheets, which can effectively increase the number of lithium-storage sites and ion diffusion rate, therefore leading to greatly enhanced energy density and cycling life.

In summary, we develop a microporous MnO_2 amorphous atomic thick sheet with crystalline vein-like support by using a simple one-step wet chemical method. The obtained unique 2D amorphous/crystalline MnO_2 structure possesses a large surface area, high porosity, and effective mechanical support, which facilitate Li-ion dynamics, accommodate volume changes, stabilize the whole structure, and enlarge the free buffering space. When evaluated as electrode materials for LIBs, this novel structure has been proved to greatly enhance reversible capacity and efficiently solves poor cycling problem of pure MnO_2 nanomaterials. It delivers extremely overlong cycle life (only fading 1% after 2500 cycles at 1A g^{-1}) and high reversible capacities (1210 mAh g^{-1} at 0.1 A g^{-1}), almost approaching the theoretical capacity of MnO_2 as an anode material for LIBs. This research not only opens a brand new pathway to prepare leaf-like homogeneous nanostructure but also provides an insight into solving poor electrochemical performance of pure metal oxide electrode materials.

Experimental Section

Synthesis of b-MnO_2 ALAT: In a typical synthesis, 8 mg $NaH_2PO_2{\cdot}H_2O$ and 10 mg $KMnO_4$ were dissolved in 20 mL deionized water, respectively. Afterwards, the $KMnO_4$ solution was slowly added to NaH_2PO_4 solution through a constant pressure titration funnel maintained at 35 °C for 0.5 h with constant stirring. The precipitate was collected after centrifugation and carefully washed with water to clean out remnant salt and subsequently dried in a freezer dryer for 24 h.

Synthesis of Amorphous MnO_2 Nanosheets: In a typical synthesis, 8 mg $NaH_2PO_2{\cdot}H_2O$ and 20 mg PVP were dissolved in 20 mL deionized water. And then, the $KMnO_4$ solution (10 mg $KMnO_4$ 20 mL deionized water) was added to NaH_2PO_2 solution through a constant pressure titration funnel maintained at 50 °C for 0.5 h. The precipitate was collected after centrifugation and carefully washed with water to clean out remnant salt and subsequently dried in a freezer dryer for 24 h.

Synthesis of Crystalline MnO_2 Nanosheets: The synthesis method is based on previous literature report.[49] In a typical synthesis procedure,

sodium dodecyl sulfate (900 mg) and sulfuric acid (0.5×10^{-3} M 300 µL) were added into 300 mL of deionized water and then heated to 90 °C in the oven. Next, $KMnO_4$ (30 mg dissolved in 30 mL of water) was quickly added into above solution to react for 3 h. The obtained solution was filtrated and the product was repeatedly washed with water and ethanol.

Characterization Morphology and Thickness Analysis: The morphology of MnO_2 plates was characterized with a scanning electron microscopy (7500F, JEOL). The TEM images were obtained with JEOL JEM-2100F at an accelerating voltage of 200 kV, and high-resolution transmission electron microscopy (HR-TEM) images and selected area electron diffraction (SAED) patterns were taken on a JEOL JEM-2100F at an accelerating voltage of 200 kV. HAADF-STEM was taken on a FEI TITAN G2 at an accelerating voltage of 300 kV. AFM was performed by a Bruker Dimension Icon. X-ray absorption spectroscopy (XAS) spectra were obtained from the Beijing Synchrotron Radiation Facility at 1W1B. The electron beam energy is 2.5 GeV and the current is between 160 and 250 mA.

Electrochemical Measurement: The anode was prepared by mixing 70 wt% of the active composite, 20 wt% of carbon black, and 10 wt% of polyvinylidene difluoride (PVDF) dissolved in *N*-methyl-2-pyrrolidone (NMP) to form slurry that then was coated on a copper foil substrate. Electrochemical tests were performed using CR2032 coin-type cells with lithium metal foil as the counter electrode. The electrolyte was 1 m LiPF6 in ethylene carbonate and diethyl carbonate (EC:DEC, 1:1 in volume), and the separator was Celgard 2300 membrane. CV tests were performed on aCHI660D electrochemical station at a current density of 0.60 mV s^{-1}, the galvanostatic discharge charge test was carried out on the LAND CT2001A battery system at room temperature.

Charge Storage Behavior for b-MnO_2 ALAT: Lithium ion intercalation kinetics can be analyzed by plotting log*(i)* versus log*(ν)* for anodic and cathodic peak currents. The measured current (*i*, A) obeys a power-law relationship with the sweep rate *ν* (mV s^{-1})

$$i = a\nu^b \tag{1}$$

Where both *a* and *b* are adjustable parameters, with *b*-values derived from the slope of the plot of log*(i)* versus log*(ν)*. In particular, a *b*-value of 0.5 indicates a diffusion-controlled process caused by cations intercalation, while $b = 1$ symbolizes a capacitive behavior via a surface faradaic redox reaction.

To distinguish quantitatively the capacitive contribution from the total current response through the voltammetric sweep rate,[50,51] Equation (1) is rewritten as

$$i(V) = k_1\nu + k_2\nu^{1/2} \tag{2}$$

Where k_1 and k_2 are adjustable values. The total current, at a fixed potential *i(V)*, is a combination of surface capacitive effects ($k_1\nu$) and diffusion-controlled processes ($k_2\nu^{1/2}$). For analytical purposes, Equation (2) can be rearranged as follows

$$i(V)/\nu^{1/2} = k_1\nu + k_2 \tag{3}$$

By plotting $\nu^{1/2}$ versus $i/\nu^{1/2}$, k_1 and k_2 can be determined from the slope and the *y*-axis intercept point.

Supporting Information

Supporting Information is available from the Wiley Online Library or from the author.

Acknowledgements

This work was financially supported by National Natural Science Foundation of China (nos. 51532001, 51872016, and 51772011).

Conflict of Interest

The authors declare no conflict of interest.

Keywords

amorphous/crystalline structure, biomimetic leaves, lithium ion batteries, 2D materials

Received: October 8, 2019
Revised: October 27, 2019
Published online:

[1] K. S. Novoselov, A. Mishchenko, A. Carvalho, A. H. Castro Neto, *Science* **2016**, *353*, aac9439.
[2] X. Wang, F. Xia, *Nat. Mater.* **2015**, *14*, 264.
[3] C. E. Boott, A. Nazemi, I. Manners, *Angew. Chem., Int. Ed.* **2015**, *54*, 13876.
[4] Y. Zhu, L. Peng, Z. Fang, C. Yang, X. Zhang, G. H. Yu, *Adv. Mater.* **2018**, *30*, 1706347.
[5] Y. Yang, X. Liu, Z. Zhu, Y. Zhong, Y. Bando, D. Golberg, J. Yao, X. Wang, *Joule* **2018**, *2*, 1075.
[6] J. Bao, X. Zhang, B. Fan, J. Zhang, M. Zhou, W. Yang, X. Hu, H. Wang, B. Pan, Y. Xie, *Angew. Chem., Int. Ed.* **2015**, *54*, 7399.
[7] S. Xu, G. Wang, B. P. Biswal, M. Addicoat, S. Paasch, W. Sheng, X. Zhuang, E. Brunner, T. Heine, R. Berger, *Angew. Chem., Int. Ed.* **2019**, *58*, 849.
[8] Z. Sun, T. Liao, W. Li, Y. Dou, K. Liu, L. Jiang, S.-W. Kim, J. Ho Kim, S. Xue Dou, *NPG Asia Mater.* **2015**, *7*, e232.
[9] P. Vukusic, J. R. Sambles, *Nature* **2003**, *424*, 852.
[10] Y. Zhang, J. Mei, C. Yan, T. Liao, J. Bell, Z. Sun, *Adv. Mater.* **2019**, https://doi.org/10.1002/adma.201902806.
[11] J. Mei, T. Liao, H. Spratt, G. A. Ayoko, X. S. Zhao, Z. Sun, *Small Methods* **2019**, *3*, 1900055.
[12] H. Cheng, Y. Zhou, Y. Feng, W. Geng, Q. Liu, W. Guo, L. Jiang, *Adv. Mater.* **2017**, *29*, 1700177.
[13] Y. Dou, D. Tian, Z. Sun, Q. Liu, N. Zhang, J. H. Kim, L. Jiang, S. X. Dou, *ACS Nano* **2017**, *11*, 2477.
[14] K. K. Sakimoto, A. B. Wong, P. Yang, *Science* **2016**, *351*, 74.
[15] H. Zhou, X. Li, T. Fan, F. E. Osterloh, J. Ding, E. M. Sabio, D. Zhang, Q. Guo, *Adv. Mater.* **2010**, *22*, 951.
[16] H. Zhang, H. Liu, Z. Tian, D. Lu, Y. Yu, S. Cestellos-Blanco, K. K. Sakimoto, P. Yang, *Nat. Nanotechnol.* **2018**, *13*, 900.
[17] W. K. Burton, N. Cabrera, F. C. Frank, *Philos. Trans. R. Soc., A* **1951**, *243*, 299.
[18] J. B. Goodenough, Y. Kim, *Chem. Mater.* **2010**, *22*, 587.
[19] V. Etacheri, R. Marom, R. Elazari, G. Salitra, D. Aurbach, *Energy Environ. Sci.* **2011**, *4*, 3243.
[20] E. H. M. Salhabi, J. Zhao, J. Wang, M. Yang, B. Wang, D. Wang, *Angew. Chem.* **2019**, *131*, 9176.
[21] J. Zhang, J. Wan, J. Wang, H. Ren, R. Yu, L. Gu, Y. Liu, S. Feng, D. Wang, *Angew. Chem., Int. Ed.* **2019**, *58*, 5266.
[22] H. Ren, R. Yu, J. Qi, L. Zhang, Q. Jin, D. Wang, *Adv. Mater.* **2019**, *31*, 1805754.
[23] C. Jiao, Z. Wang, X. Zhao, H. Wang, J. Wang, R. Yu, D. Wang, *Angew. Chem.* **2019**, *131*, 1008.
[24] D. Mao, J. Wan, J. Wang, D. Wang, *Adv. Mater.* **2019**, *31*, 1802874.
[25] S. Wang, Q. Wang, P. Shao, Y. Han, X. Gao, L. Ma, S. Yuan, X. Ma, J. Zhou, X. Feng, B. Wang, *J. Am. Chem. Soc.* **2017**, *139*, 4258.
[26] R. Bi, G. Liu, C. Zeng, X. Wang, L. Zhang, S. Z. Qiao, *Small* **2019**, *15*, 1804958.

[27] D. Chao, W. Zhou, C. Ye, Q. Zhang, Y. Chen, L. Gu, K. Davey, S. Z. Qiao, *Angew. Chem., Int. Ed.* **2019**, *58*, 7823.
[28] F. Jiao, P. G. Bruce, *Adv. Mater.* **2007**, *19*, 657.
[29] Y. Min, G. D. Moon, B. S. Kim, B. Lim, J. S. Kim, C. Y. Kang, U. Jeong, *J. Am. Chem. Soc.* **2012**, *134*, 2872.
[30] F. Wang, J. H. Seo, G. Luo, M. B. Starr, Z. Li, D. Geng, X. Yin, S. Wang, D. G. Fraser, D. Morgan, Z. Ma, X. Wang, *Nat. Commun.* **2016**, *7*, 10444.
[31] P. Yang, Y. Ding, Z. Lin, Z. Chen, Y. Li, P. Qiang, M. Ebrahimi, W. Mai, C. P. Wong, Z. L. Wang, *Nano Lett.* **2014**, *14*, 731.
[32] Y. Zhao, C. Chang, F. Teng, Y. Zhao, G. Chen, R. Shi, G. I. N. Waterhouse, W. Huang, T. Zhang, *Adv. Energy Mater.* **2017**, *7*, 1700005.
[33] P. Gao, P. Metz, T. Hey, Y. Gong, D. Liu, D. D. Edwards, J. Y. Howe, R. Huang, S. T. Misture, *Nat. Commun.* **2017**, *8*, 14559.
[34] M. Kundu, C. C. A. Ng, D. Y. Petrovykh, L. Liu, *Chem. Commun.* **2013**, *49*, 8459.
[35] Y. Jiang, D. Zhang, Y. Li, T. Yuan, N. Bahlawane, C. Liang, W. Sun, Y. Lu, M. Yan, *Nano Energy* **2014**, *4*, 23.
[36] C. Zhao, H. Zhang, W. Si, H. Wu, *Nat. Commun.* **2016**, *7*, 12543.
[37] Y. Huang, Z. Xu, J. Mai, T.-K. Lau, X. Lu, Y.-J. Hsu, Y. Chen, A. C. Lee, Y. Hou, Y. S. Meng, Q. Li, *Nano Energy* **2017**, *41*, 426.
[38] H. Sun, G. Xin, T. Hu, M. Yu, D. Shao, X. Sun, J. Lian, *Nat. Commun.* **2014**, *5*, 4526.
[39] S. Okuoka, Y. Ogasawara, Y. Suga, M. Hibino, T. Kudo, H. Ono, K. Yonehara, Y. Sumida, Y. Yamada, A. Yamada, M. Oshima, E. Tochigi, N. Shibata, Y. Ikuhara, N. Mizuno, *Sci. Rep.* **2015**, *4*, 5684.
[40] L. Li, A. R. Raji, J. M. Tour, *Adv. Mater.* **2013**, *25*, 6298.
[41] C. X. Guo, M. Wang, T. Chen, X. W. Lou, C. M. Li, *Adv. Energy Mater.* **2011**, *1*, 736.
[42] D. Kong, J. Luo, Y. Wang, W. Ren, T. Yu, Y. Luo, Y. Yang, C. Cheng, *Adv. Funct. Mater.* **2014**, *24*, 3815.
[43] J. Y. Liao, D. Higgins, G. Lui, V. Chabot, X. Xiao, Z. Chen, *Nano Lett.* **2013**, *13*, 5467.
[44] A. L. M. Reddy, M. M. Shaijumon, S. R. Gowda, P. M. Ajayan, *Nano Lett.* **2009**, *9*, 1002.
[45] H. Lai, J. Li, Z. Chen, Z. Huang, *ACS Appl. Mater. Interfaces* **2012**, *4*, 2325.
[46] J. Zhou, T. Yang, M. Mao, W. Ren, Q. Li, *J. Mater. Chem. A* **2015**, *3*, 12328.
[47] M. Zhong, D. Yang, C. Xie, Z. Zhang, Z. Zhou, X. H. Bu, *Small* **2016**, *12*, 5564.
[48] Z. Y. Sui, C. Wang, K. Shu, Q.-S. Yang, Y. Ge, G. G. Wallace, B.-H. Han, *J. Mater. Chem. A* **2015**, *3*, 10403.
[49] S. Chen, J. Duan, A. Vasileff, S. Z. Qiao, *Angew. Chem., Int. Ed.* **2016**, *55*, 3804.
[50] J. Wang, J. Polleux, J. Lim, B. Dunn, *J. Phys. Chem. C* **2007**, *111*, 14925.
[51] Z. Chen, V. Augustyn, X. Jia, Q. Xiao, B. Dunn, Y. Lu, *ACS Nano* **2012**, *6*, 4319.

